

# Role of Dynamical Heterogeneities on the Viscoelastic Spectrum of Polymers: A Stochastic Continuum Mechanics Model

Robin J. Masurel,<sup>†</sup> Sabine Cantournet,<sup>‡</sup> Alain Dequidt,<sup>¶</sup> Didier R. Long,<sup>§</sup> H el ene Montes,<sup>\*,†</sup> and Fran ois Lequeux<sup>†</sup>

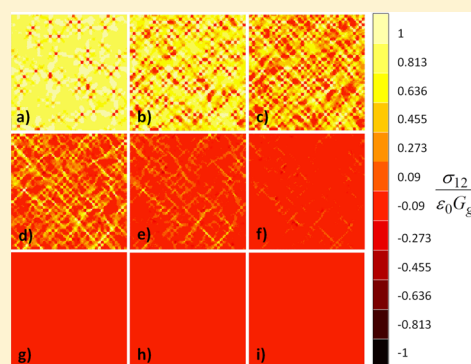
<sup>†</sup>CNRS UPMC ESPCI ParisTech PSL Res Univ, Lab SIMM, UMR 7615, F-75231 Paris, France

<sup>‡</sup>MINES ParisTech, PSL-Research University, MAT - Centre des mat eriaux, CNRS UMR 7633, BP 87 91003 Evry, France

<sup>¶</sup>Univ Clermont Ferrand, Inst Chim Clermont Ferrand, UMR 6296, F-63171 Aubiere, France

<sup>§</sup>Laboratoire Polym eres et Mat eriaux Avanc es, UMR 5268 CNRS/Solvay, 87, rue des fr eres Perret, F-69192 Saint Fons, France

**ABSTRACT:** Amorphous polymers in their glass transition regime can be described as a tiling of nanometric domains. Each domain exhibits its own relaxation time, which is distributed over at least four decades. These domains are known as dynamical heterogeneities. This article describes the mechanics of amorphous polymers using a stochastic continuum mechanics model that includes their heterogeneous dynamics. Solving this model both by finite elements and by using a self-consistent method, we find a viscoelastic relaxation spectrum quantitatively similar to an experimentally measured spectrum in a polymer. We show evidence that elastic couplings between domains control the stress relaxation after a step strain and result in a narrowing of the long-time region of the viscoelastic spectrum (as compared to that of dynamical heterogeneities).



## INTRODUCTION

A glassy polymer is characterized by a dense and highly disordered packing of monomers. Disorder results from structural constraints, namely excluded volume, but also connectivity between monomers, entanglements, or cross-links. The monomers rearrange collectively by small domains, hopping from one configuration to another, or one cage to another in the Eyring model.<sup>1</sup> As shown two decades ago,<sup>2–9</sup> one consequence of the structural disorder is the strong heterogeneity of polymer chain dynamics at a nanometric scale. Molecular dynamics (MD) simulations and experiments using photobleaching have shown that the mechanical properties of glasses are heterogeneous at a nanometric length scale.<sup>10–14</sup> More precisely, the rearrangement rate varies by orders of magnitude from one domain to another.<sup>15</sup>

At high temperature, in the melt regime, the rearrangement times of nanometric domains are short compared to the time of the experiment. The mechanical response of dense polymer chains is thus controlled by long-range topological constraints, such as entanglements or cross-links, and is characterized by an elastic modulus of the order of 1 MPa.

At low temperature, in the glassy state, the experimental time is longer than local relaxation times. The dynamics of polymers is controlled by rare rearrangements of monomers. In this range of temperatures, elasticity results from interactions between monomers and the elastic modulus is of the order of 1 GPa.

Close to the glass transition, the situation is more complex because the polymer system is composed of nanometric domains having relaxation times either shorter or longer than

the experimental time. The former can differ by at least four orders of magnitude between two neighboring domains.<sup>2</sup>

For instance, during a step strain mechanical test, each domain releases its stress with a characteristic time, which can be significantly different from that of its neighbors. During its relaxation, the local modulus of each domain will typically vary by three orders of magnitude from 1 GPa to 1 MPa. As a consequence, the local stresses are highly distributed within the sample, depending on the local value of the relaxation time. The corresponding macroscopic stress relaxation should be influenced by this huge dynamical disorder. However, its quantitative description is still a challenge.

This work aims at evidencing the relation between local stress relaxation and the macroscopic viscoelastic modulus measured in the linear regime close to the glass transition. An important issue concerns the arrangement of mechanical heterogeneities and its evolution during macroscopic relaxation. The complexity of the situation originates in the elastic coupling between the domains interacting together elastically. This coupling may lead to complicated local stress relaxations partly controlled by the initial dynamical arrangement as observed by Yoshimoto et al.<sup>18</sup> For instance, stress localization may occur as a result of mechanical couplings. A better understanding of the effect of dynamical heterogeneities on the macroscopic response of a polymer glass would be helpful for

**Received:** May 27, 2015

**Revised:** July 24, 2015

**Published:** September 3, 2015

the development of new highly heterogeneous polymer systems.

Mechanical properties of glasses have been studied by molecular dynamics simulations.<sup>12</sup> However, MD analysis is typically restricted to time scales shorter than 1  $\mu$ s and sample sizes smaller than 100 domains. Because the full relaxation of a glassy polymer occurs over macroscopic times larger than 1 s, MD simulations therefore do not allow one to study the mechanical response of a polymer relaxing from its glassy to its rubber state. Recently, Dequidt et al.<sup>15</sup> have developed a more appropriate model using a coarse-grained Monte Carlo (CGMC) simulation technique. This CGMC model is based on the “percolation of free volume distribution” (PFVD)<sup>16,17,19</sup> theory and includes the dynamical heterogeneities that are induced by the density fluctuations existing in a polymer glass. In this CGMC model, local stresses intermittently relax from the glassy to the rubber state in such a way that physical aging is taken into account. This model gives a good description of the mechanical properties of confined polymer films close to their glass transition.

Previous works have not analyzed the spatial correlations of the stress field that take place during the macroscopic relaxation of the glassy system. Nevertheless, these local stress correlations control the macroscopic response of a glassy polymer. In order to get new insight on the relaxation processes occurring at a local scale, we have developed a numerical technique that is faster than the CGMC model. In this work, we use a finite element method (FE) because this method has been optimized for decades in order to solve mechanical response of heterogeneous systems.<sup>20–22</sup> For that purpose, we implemented statistical physics of the  $\alpha$  relaxation of a polymer glass in a finite element computation. We show in this paper how to easily implement the statistical behavior associated with glass transition in finite element codes. This finite element approach takes the intrinsic dynamical heterogeneities existing in a polymer into account. For that purpose, we assume a Maxwellian viscoelastic response for each domain considered individually. As a consequence, the domains undergoing a constant strain would relax from a glassy modulus to a rubbery modulus following a single exponential decay. In the model presented in this article, we choose to keep constant the intrinsic relaxation time of each domain during the whole macroscopic stress release. The physical aging processes are thus not taken into account. They will be included in a further development of this model.

Using this new numerical method, we have modeled polymer mechanics at the nanometric scale of dynamical heterogeneities. In particular, we were able to analyze macroscopic stress with respect to the distribution of local stresses and their spatial correlation at each macroscopic relaxation time. In order to get insight into the spatial arrangement of domains' relaxation, FE results were compared to the ones given by a self-consistent mechanical (Palierne) model (SC). In this paper, we present the resulting predictions for a two-dimensional (2D) plane strain geometry.

This paper is organized as follows. In the first section, details of the FE and SC numerical methods we used are presented. We have studied the sensitivity of the FE technique in this statistical physics problem, particularly in the case of polymer glasses in which intrinsic relaxation time distributions are very broad (over 8–16 decades). The macroscopic stress relaxations predicted by FE simulations are reported in a second section. Their shape strongly depends on the width,  $\sigma$ , of the intrinsic

time distribution and on the mechanical contrast,  $G_g/G_r$ , between the glassy and the rubber state. FE simulations are compared to the macroscopic response predicted by a mean field approach. We show that, in the glass transition zone, mean field approach overestimates macroscopic stress relaxation for heterogeneous systems. This discrepancy between FE and SC predictions reveals the existence of a complex time evolution of the stress field during the macroscopic relaxation in polymer glasses. By analyzing the corresponding local stress field predicted by FE simulations at each step of the macroscopic relaxation, we have identified four main steps in the relaxation kinetics of local stresses and their spatial organization within the sample. The role of elastic couplings on the stress relaxation of domains is discussed in the third section. We show that elastic couplings induce a long-range spatial arrangement of the local stress (cf. first subsection) and modify the local stress relaxation kinetics (cf. second subsection). The range of these spatial and dynamical correlations are analyzed during macroscopic relaxation. Lastly, we compare in a third subsection the time distribution deduced from the rheological measurements of a polymer glass to the intrinsic time distribution. We show that mechanical couplings significantly decrease the weights of the longest time of the intrinsic time distribution. Using finite element simulations allows for an understanding of the physics of the  $\alpha$  relaxation of a polymer. This work is the first step toward a quantitative modeling of the  $\alpha$  relaxation viscoelastic and elasto-visco-plastic behavior of polymers in their glass transition regime.

## ■ INTRODUCTION OF THE MODEL

**Classical Picture of Glass Dynamics.** This work aims at modeling dynamical heterogeneities and their consequences on the viscoelastic spectrum of the  $\alpha$  relaxation using finite elements. The picture is now well-established qualitatively: In its glass transition regime, a polymer can be considered as constituted of nanometric domains, the sizes of which weakly vary with temperature.<sup>16,23</sup> Each domain has a specific lifetime and thus may randomly hop in a new configuration. In the presence of stress, hopping goes together with, on average, a release of the stress, as described by the Eyring model. In its new configuration, it gets a new lifetime. The important point is that lifetimes are distributed over many decades, as proven by various experiments.<sup>2</sup>

Let us now consider the  $\alpha$  relaxation of a polymer after a step strain. Prior to macroscopic relaxation, each domain is glassy and relaxes following his initial lifetime,  $\tau_i$ . When the lifetime of a given domain is elapsed, the domain hops in a new arrangement with a vanishing stress, and its lifetime is changed. At the end of the relaxation, or over a long time scale, all domains have hopped, possibly several times, and the matrix has a rubbery modulus. In order to describe the physics of this relaxation, as well as dynamical heterogeneities, we introduce the model described in the following.

**Model.** Space is divided in domains, each differing by its own mechanical response with a lifetime  $\tau_i$  (as shown in Figure 1).

The response of each domain is glassy at short times. Instead of describing a hop in the stress–strain relation, we assume that each domain exhibits an exponential decay of the stress. Note that for a large number of domains, a random hop with a given lifetime is equivalent to an exponential decay. Indeed, replacing the hopping by an exponential decay, we lose the stepwise stress relaxation that may be observed on very small systems. However, by doing so, each domain can be replaced by a Maxwell element. Second, we assume that the lifetime of a domain remains constant with the elapsed time. We believe it is a relevant approximation because in a step strain relaxation, most of the stress has relaxed during the first decay of the stress. Lastly, we place in parallel to the Maxwell element a spring that accounts for rubber elasticity and which is relevant at long time scale.

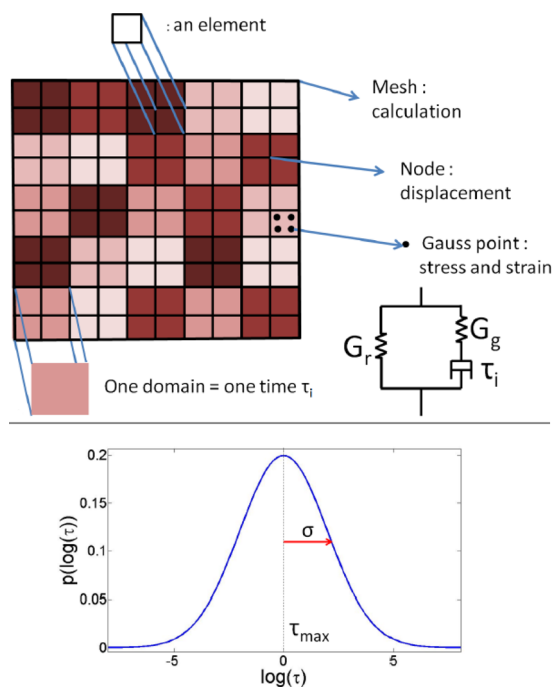


**Figure 1.** Dynamical heterogeneities in a polymeric glass. Introduction of a finite element method. Each colored square of four elements represents a domain which has the same mechanical behavior.  $G_g$  and  $G_r$  are constant over the whole sample.

We assume for the sake of simplicity that the material is incompressible; in practice, the bulk modulus is of the order of 1 GPa, and we have checked that the overall response is not significantly sensitive to the bulk modulus in the plain strain condition. This model has two major advantages. First, it is simple to implement in a finite element software; second, a self-consistent estimate of the viscoelastic spectrum can also easily be performed.

Hence, the polymer system is considered as a set of unit domains  $i$ , each one having its own mechanical response characterized by a complex modulus  $G_i^*$ . (Unit domains are arbitrarily represented by squares in Figure 1.) As explained above, the modulus  $G_i^*$  of each domain  $i$  is given by a generalized Maxwell model where moduli  $G_g$  and  $G_r$  are the glassy and rubbery shear moduli, respectively, of a polymeric material with a single characteristic relaxation time,  $\tau_i$ , that can be simply written as

$$G_i^*(\omega) = G_g \frac{i\omega\tau_i}{1 + i\omega\tau_i} + G_r \quad (1)$$

In this work,  $G_g$  and  $G_r$  are constant for all unit domains of a given system.  $G_g$  was taken to be equal to 1 GPa, which is approximately the modulus value of glassy polymer chains.  $G_r$  was varied from  $G_r = 0$  to  $10^{-1}G_g$ . Most simulations were performed taking  $G_r = 10^{-3}G_g$ , which corresponds to a typical value for the modulus of a rubber polymer matrix. The relaxation times  $\tau_i$  are distributed over all unit domains according to a distribution  $p(\tau_i)$ . Indeed, at small scales, a polymer glass exhibits fluctuations of packing, density, and arrangement. These fluctuations may induce a Gaussian distribution of the energy barriers involved in the  $\alpha$  relaxation. As the relaxation time strongly depends, typically exponentially, with the barrier height, it is likely that the time distribution is log-normal. We thus choose a log-normal distribution for  $p(\tau_i)$ :

$$p(\log(\tau_i)) = \frac{1}{\sqrt{(2\pi)\sigma}} \exp\left(-\frac{(\log(\tau_i) - \log(\tau_{\max}))^2}{2\sigma^2}\right) \quad (2)$$

where  $\log(\tau_{\max})$  is the center of the log-normal time distribution. We define the dimensionless time  $t^* = t/\tau_{\max}$ . In eq 2,  $\sigma$  is the standard deviation of the log-normal distribution of times, which has been

taken equal to either 2 or 4.<sup>24,25</sup> For real homopolymers, we would expect  $\sigma$  values around 2, while for blends of two asymmetric miscible polymers having very different  $T_g$ ,  $\sigma$  would be larger and could reach a value around 4. In this model, there are two dimensionless parameters: the ratio  $G_r/G_g$  and the width of the time distribution  $\sigma$ .

We will now compute both macroscopic viscoelastic response and microscopic behavior using finite elements and a self-consistent resolution in plain strain for an incompressible medium under a small deformation. In this case, simple shear and pure shear are equivalent in the determination of the macroscopic shear modulus. In the following, we study the case of a simple shear, and eigendirections of the applied macroscopic strain tensor are oriented at  $45^\circ$  from horizontal.

**Self-Consistent Method.** From the microscopic constitutive equations distribution ( $G_i^*(\omega)$ ), it is possible to first apply the self-consistent method of homogenization for viscoelastic materials. The homogenized elastic shear modulus of 2D inclusions (aligned fibers originally) in the plane strain condition is presented in ref 26. Masson and Zaoui extended the three-dimensional (3D) elastic calculation to viscoelastic inclusions and matrix using a Laplace transform.<sup>27</sup> This work has been used for viscoelastic emulsions taking into account the surface tension<sup>28</sup> and more recently for polymer systems.<sup>24</sup> The same extension is done for 2D inclusions here. We first consider the complex modulus of a homogeneous matrix of modulus  $G_m^*$  containing a small volume fraction of various viscoelastic spherical inclusions of complex modulus  $G_i^*$ . The macroscopic modulus of the sample  $G^*$  in the incompressible self-consistent case is given by eq 3.

$$G^* = G_m^* \left[ 1 - \Phi \int_{\tau_i} p(\tau_i) \frac{G_i^*(G_m^* - G_i^*)}{G_m^*(G^* - G_i^*)} \left( \frac{G_m^*}{G_m^* - G_i^*} - \frac{1}{2} \right)^{-1} d\tau_i \right] \quad (3)$$

In eq 3,  $\Phi$  is the total volume fraction of inclusions and  $p(\tau_i)$  is the characteristic time distribution of the inclusions such that  $\int_{\tau_i} p(\tau_i) d\tau_i = 1$ .

We will now make an analogy between our system composed only of a tiling of domains and a matrix containing various inclusions. Let us consider a homogeneous matrix with the viscoelastic modulus  $G_m^*$ . Let us now consider this same homogeneous matrix, but containing inclusions, with a total volume fraction  $\Phi$  that exhibits the same distribution of mechanical properties as the heterogeneous system. We are seeking a homogeneous matrix having the same mechanical properties as the heterogeneous system  $G^*$ . In this case, whether the matrix contains representative inclusions or not has not to change  $G_m^*$ .

This leads thus to  $G^* = G_m^*$ . Whatever the value of  $\Phi$ , this additional condition changes eq 3 into

$$\int_{\tau_i} p(\tau_i) \frac{G_{i,2D}^* - G_{2D}^*}{G_{i,2D}^* + G_{2D}^*} d\tau_i = 0 \quad (4)$$

This relation ensures that, in the frame of the self-consistent approach  $G^* = G_{2D}^* = G_{m,2D}^*$ . Equation 4 can then be numerically solved<sup>24</sup> to obtain  $G^*$ .

This mean field approximation allows us to estimate the average macroscopic response of a heterogeneous system. This self-consistent model assumes that a given domain is embedded in a matrix that is considered to be homogeneous (mean field). But in reality a domain is embedded, not in a homogeneous matrix, but in a limited number of domains with heterogeneous mechanical properties. These correlations may eventually affect its local stress relaxation. In this case we should observe a difference between the self-consistent result and the exact mechanical response. As a result, one can wonder what should be the mechanical response of a heterogeneous system at the scale of a domain.<sup>29</sup> To answer this question, we have developed a finite element method, presented in the next section.

**Finite Element Method.** In this section, we detail the way the stochastic finite element method is implemented and its robustness ensured. Readers not interested in this point may skip directly to Results.

**Implementation of the Finite Element Method.** The finite element method is a procedure for obtaining numerical approximations to the

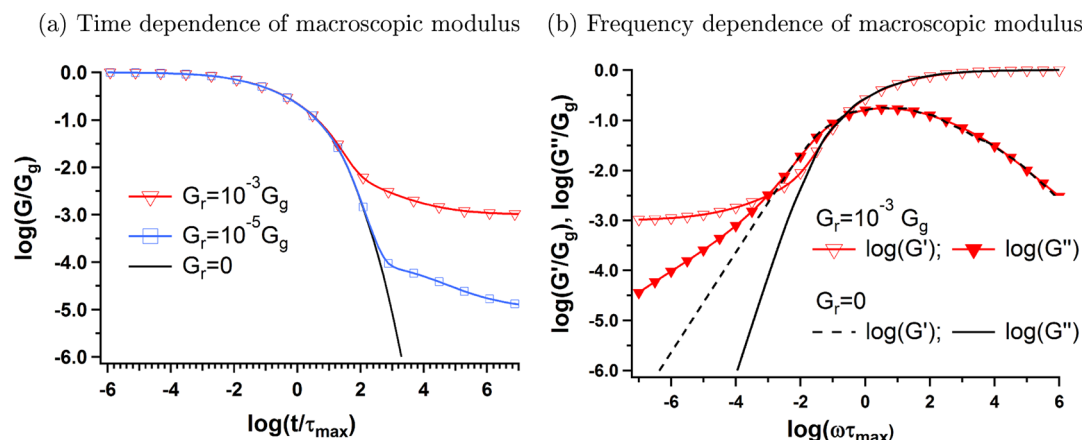


**Figure 2.** Logarithmic variation of modulus  $G$  with  $\log(t/\tau_{\max})$  (a) or with  $\log(\omega\tau_{\max})$  (b). Data were calculated for  $\sigma = 2$  and  $G_r = 0$  (black),  $G_r = 10^{-5}G_g$  (blue), or  $G_r = 10^{-3}G_g$  (red).

solution of boundary value problems posed over a domain. This domain is replaced by the union of disjoint subdomains called finite elements or elements in a shortened form. Here we attribute to each element an intrinsic relaxation time  $\tau_i$ . The response of each element is expressed in terms of a finite number of degrees of freedom characterized as the value of an unknown function at a set of nodal points. The stresses in each element are related to the strains by use of the time integral equation of 1:

$$\sigma(t) = \int_0^t C_r \frac{\partial \epsilon(s)}{\partial s} ds + \int_0^t C_g e^{-t/\tau_i} \frac{\partial \epsilon(s)}{\partial s} ds \quad (5)$$

The subscripts  $r$  and  $g$  will denote rubber and glassy components, respectively.  $C_r$  and  $C_g$  are fourth-order material tensors. Assuming isotropy, these take the reduced form  $C_i = 2\mu_i \mathbf{I} \otimes \mathbf{I} + \lambda_i \mathbf{l}$ , where  $\mu$  and  $\lambda$  are the scalar, Lamé coefficients and  $\mathbf{I}$  is the second-order identity tensor;  $\mathbf{l}$  is the symmetric order of the fourth-rank identity tensor.

Because the problem is nonlinear in time step, an iterative procedure should be followed in order to ensure equilibrium in each time increment. Here the Newton–Raphson method was used for that purpose.

In summary, we divide the structure into elements with nodes attributing a time  $\tau_i$  to each element. We use periodic boundary conditions, and we solve it in time, using logarithmic time step, in order to cover about 12 decades of time using the ZeBuLon FE software.<sup>30,31</sup> As specified in the precedent section, we work in the 2D plane strain condition. The medium is incompressible at all frequencies; in practice, we fix the bulk modulus  $K = 10^5 G_g$ .

**$G'$  and  $G''$  Calculations.** For all finite element simulations, we impose a macroscopic shear step strain  $\epsilon_{12} = \epsilon_0 = 0.01$  (which is consistent with small deformation condition used in the model), and the time relaxation of the macroscopic stress  $\sigma_{12}(t)$  is computed. Calculations were performed over a large enough time range such that the whole stress relaxation can be observed. We calculated 8 and 3 stress values per time decade for the simulations with  $\sigma = 2$  and  $\sigma = 4$ , respectively.

We deduce the frequency-dependent macroscopic complex modulus  $G^*(\omega)$  from the macroscopic stress relaxation curve  $\sigma_{12}(t)$ . In order to do so, we assume that the macroscopic stress  $\sigma_{12}(t)$  fits to a sum of the Maxwellian response of each unit domain (cf. eq 6) with the normalized  $F(\tau)$  distribution function.

$$\sigma_{12}(t) = \int_0^\infty F(\tau)(G_g e^{-t/\tau} + G_r) d\tau \quad \text{with} \quad \int_0^\infty F(\tau) = 1 \quad (6)$$

This is indeed equivalent to a Fourier transform. In practice, we use a discrete function  $F(\tau)$  setting 50 values of  $\tau$  for  $\sigma = 2$  and 100 for  $\sigma = 4$ . From the  $F(\tau)$  function determined by the previous  $\sigma_{12}(t)$  fit, we deduce the macroscopic complex modulus  $G^*(\omega)$  according eq 7.

$$G^*(\omega) = \int_0^\infty F(\tau) \left( G_g \frac{i\omega\tau}{1 + i\omega\tau} + G_r \right) d\tau \quad (7)$$

Figure 2a presents the typical curves obtained for the time dependence of the shear modulus  $G(t)$  for  $\sigma = 2$  and taking  $G_r = 0$  (corresponding to unentangled polymer chains) or  $G_r = 10^{-3}G_g$  (typical of entangled or cross-linked polymer chains). The corresponding frequency dependence of the complex modulus  $G^*(\omega)$  is presented in Figure 2b.

**Representative Volume Element Definition and Characterization.** Unlike standard finite elements, and because we use here a random set of  $\tau_i$  values, the estimation of the minimal size of the finite element simulations has to be discussed precisely. Computations have to be performed on a large enough volume such that results are representative of the mechanical response of a macroscopic sample. Therefore, we need to define the minimum number of domains  $N$  required for a tiling to be representative of a bulk sample. First, the random draw of the  $\tau_i$  values induces a variance on the shear modulus that decreases with the number of domains.  $N$  has to be large enough for the variance to be reasonably small. Second, the mechanical average depends on the size of the sample. The number of domains has to be large enough so that edge effects are negligible. Thus, as  $N$  increases, the mean value of  $G'_N(\omega\tau_{\max})$ ,  $\langle G'_N(\omega\tau_{\max}) \rangle$ , calculated from different  $\tau_i$  distributions, tends toward the macroscopic modulus  $G'_\infty(\omega\tau_{\max})$  corresponding to a sample of an infinite size, while its variance  $(\langle G'_N(\omega\tau_{\max}) \rangle^2 - G'_N(\omega\tau_{\max})^2)$ , tends toward zero.

To estimate the ideal size of the system, the modulus was calculated varying  $N$ . For each sample of size  $N$ , ten  $\tau_i$  draws in agreement with eq 2 were used. From these, we deduce the modulus average  $\langle G'_N(\omega\tau_{\max}) \rangle$  and the standard deviation  $\sigma_N$ . Figure 3 shows the typical variation of  $\langle G'_N \rangle$  for increasing  $N$  obtained at a given frequency

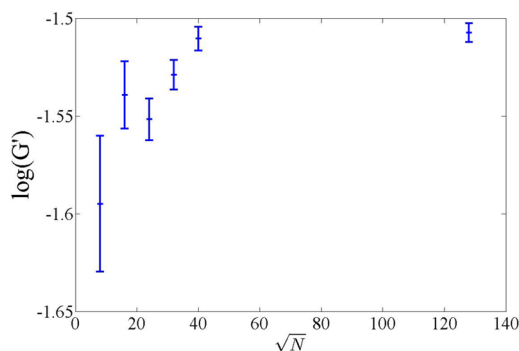


**Figure 3.** Variation of the logarithm of elastic modulus  $G'$  at  $\log(\omega\tau_{\max}) = -1.6$  versus the domain number  $N$ . Simulations were performed taking  $\sigma = 2$  and  $r = 2$ .

$\log(\omega\tau_{\max}) = -1.4$  for a time distribution width  $\sigma = 2$ . For  $\sqrt{N} > 20$ , the standard deviation becomes negligible. Moreover,  $\langle G'_N \rangle \approx G'_N \approx G'_\infty$  for  $\sqrt{N} > 40$ . We checked that a size of  $N = 40 \times 40$  domains is also ideal for a larger time distribution width  $\sigma = 4$ . In this work, we thus took  $N = 40 \times 40$  domains for all finite element simulations.

**Effect of the Number of Elements by Domain.** If the number of elements,  $N_{el}$ , describing a single domain is too small, there are not enough degrees of freedom and the system appears stiffer than it should be. We tested different ratios between the number of elements and the number of domains. We define the quantity  $r = \sqrt{\frac{N_{el}}{N}}$ . In Figure 4, it appears that  $r = 2$  (4 elements by domain) is sufficient for  $\sigma = 2$ . The same analysis leads to fix  $r = 4$  (16 elements by domain) for  $\sigma = 4$ .

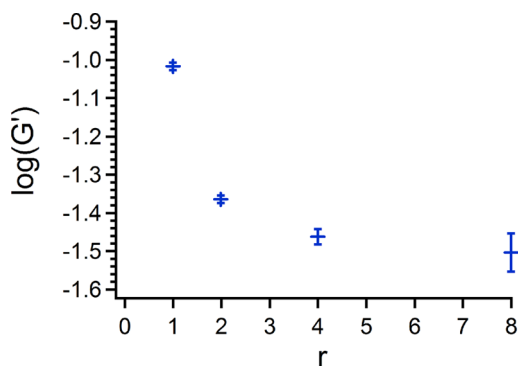


**Figure 4.** Variation of logarithm of elastic modulus  $G'$  at  $\log(\omega\tau_{\max}) = -1.6$  versus  $r = \sqrt{\frac{N_{el}}{N}}$ . Simulations were performed taking  $\sigma = 2$  and  $N = 128 \times 128$  for  $r = 1$ ,  $r = 2$ , and  $r = 4$ . For  $r = 8$ ,  $N = 64 \times 64$ .

## RESULTS

Figure 5 presents the  $G^*(\omega)$  curves obtained by the finite element method for  $\sigma = 2$ .  $G_r$  values were vary from  $10^{-1} G_g$  to  $10^{-7} G_g$  from top to bottom. On Figure 6 are displayed the results obtained for  $\sigma = 4$ . We observe that on the high-frequency side of the glass transition, the complex moduli  $G^*(\omega)$  are similar whatever the value of  $G_r$ . The broadness of the loss modulus maximum significantly depends on the width of time distribution  $\sigma$ , as clearly seen when comparing Figures 5 and 6. In addition, for vanishing values of  $G_r$ , the behavior is Maxwellian:  $G'$  scales as  $\omega^2$  and  $G''$  scales as  $\omega$ . For larger values of  $G_r$ , that low-frequency scaling is not verified provided

$G'(\omega) < 10G_r$ . A pseudorubber plateau can appear in the low-frequency side of the glass transition (for example, this pseudoplateau regime lies between  $\log(\omega) = -4.5$  and  $-3$  for  $\sigma = 2$  and  $\frac{G_g}{G_r} = 10^5$ ) and is followed at very low frequencies by a true plateau equal to  $G_r$ . The pseudoplateau regime is particularly visible for low values of  $\sigma$  and high values of  $\frac{G_g}{G_r}$ .

**Comparison with Self-Consistent Approximation.** First we will compare the responses predicted by finite element method to the ones given by the self-consistent approximation. In Figure 7, data obtained for  $\sigma = 2$  and  $G_r = 10^{-3} G_g$  are displayed. Series (or Voigt) and parallel (or Reuss) approximations, which correspond to strain and stress averages, respectively, are also plotted in Figure 7. We observe that series and parallel models are very poor approximations of the exact calculation made by the finite element method. This can be explained by the very large time distribution on one hand, and by the high moduli contrast between  $G_g$  and  $G_r$  on the other hand.

The self-consistent approximation leads to much more accurate  $G'$  and  $G''$  curves. However, deviations from finite element predictions appear in the glass transition domain, the amplitude of which depends on the two physical parameters of the model: the modulus contrast between the rubber and the glassy state  $\frac{G_g}{G_r}$  and the intrinsic relaxation time distribution

width  $\sigma$ . First, Figure 8 compares the predictions given by the finite element and the self-consistent approaches for varying time distribution width  $\sigma$ . Calculations were performed assuming  $G_r = 10^{-3} G_g$ . Both methods yield the same macroscopic modulus values  $G^*(\omega)$  when approaching both the rubber and glassy limits. However, their predictions differ in the glass transition domain. On Figure 8, deviations between self-consistent and finite elements predictions spread over four frequency decades for  $\sigma = 2$  and eight frequency decades for  $\sigma = 4$ . The larger the time distribution, the larger the amplitude of the discrepancy. In addition, the broadness of the glass transition domain clearly increases with  $\sigma$ . As a consequence, the slope of the frequency dependence of the modulus decreases as  $\sigma$  increases. Figure 9 compares the maximum value of the elastic modulus slope, denoted  $\max\left(\frac{\partial \log(G')}{\partial \log(\omega)}\right)$ , observed for varying  $\sigma$ . As expected, for a constant value of  $\frac{G_g}{G_r}$ ,

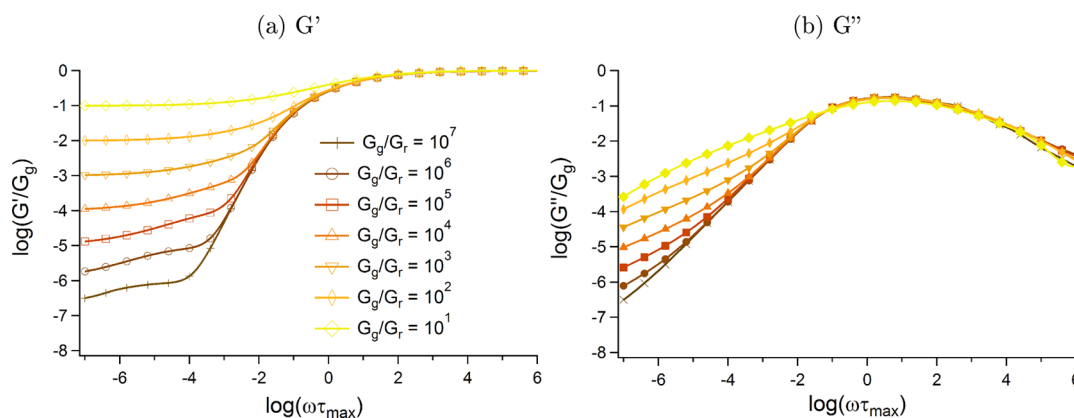


**Figure 5.** Frequency dependence of elastic part  $G'(\omega)$  (a) and loss part  $G''(\omega)$  (b) of the macroscopic modulus of a heterogeneous system. Simulations were performed taking  $\sigma = 2$ .  $\frac{G_g}{G_r}$  was varied from 10 to  $10^7$  with step of one decade (top curve to bottom curve).

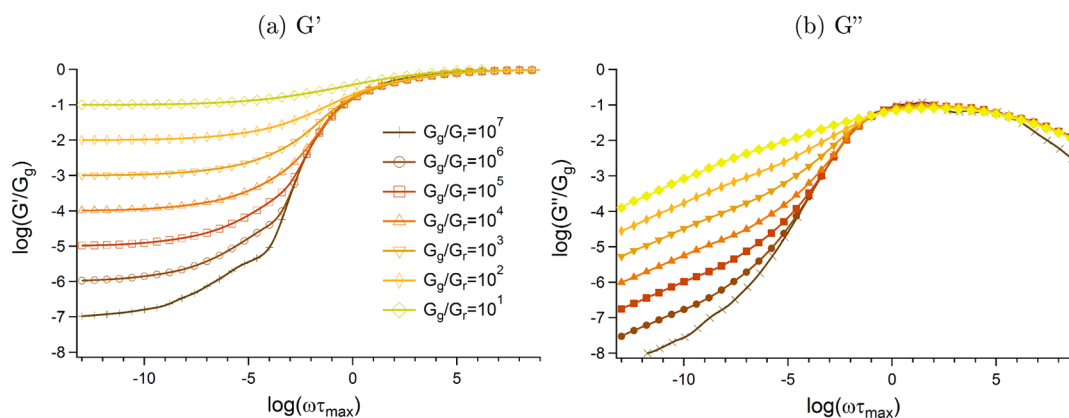


**Figure 6.** Frequency dependence of elastic part  $G'(\omega)$  and loss part  $G''(\omega)$  of the macroscopic modulus of a heterogeneous system.  $\frac{G_g}{G_r}$  was varied from 10 to  $10^7$  with step of one decade (top curve to bottom curve).

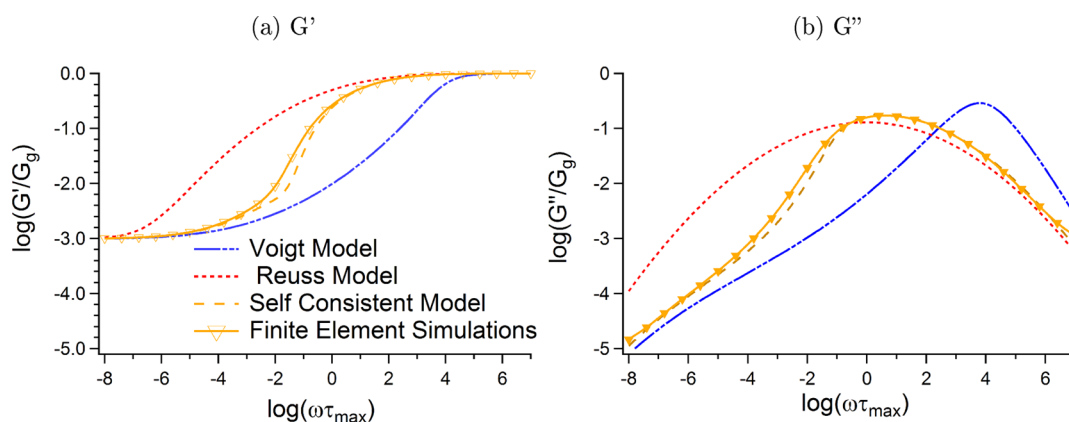


**Figure 7.** Series model, parallel model, self-consistent model, and finite element calculation comparison for  $\sigma = 2$  and  $\log\left(\frac{G_g}{G_r}\right) = 3$ .

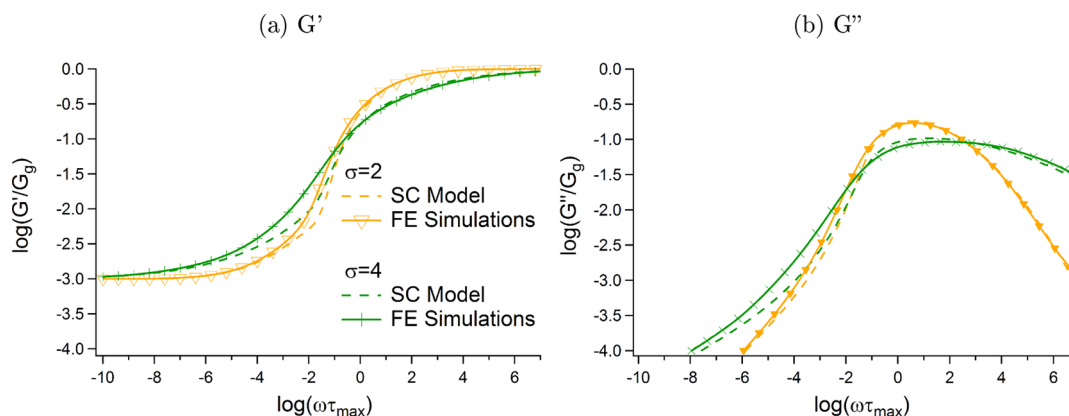


**Figure 8.** Frequency dependence of elastic modulus  $G'(\omega)$  and loss modulus  $G''(\omega)$  predicted by 2D self-consistent model (dotted line) and 2D finite element model (line) for 2D finite element simulation  $G_r = 10^{-3}G_g$  and varying time distribution width  $\sigma$ . Yellow data correspond to  $\sigma = 2$ , green data to  $\sigma = 4$ .

$\max\left(\frac{\partial \log(G')}{\partial \log(\omega)}\right)$  decreases for increasing time distribution width  $\sigma$ . Moreover, the self-consistent approximation predicts a larger maximal slope for the elastic part of the modulus. Hence, the self-consistent model underestimates the width of the macroscopic relaxation, as explained further below. We have added experimental data deduced from mechanical measurements performed on homopolymers or asymmetric miscible polymer blends having a very broad glass transition domain. According

to these results, the width of the time distribution function should be around 2 for homopolymers and could reach a value of 4 for asymmetric miscible blends (assuming 2D simulations capture the width of the glass transition of 3D experimental systems, which seems reasonable).

*Influence of the Modulus Contrast  $G_g/G_r$ .* The discrepancies with finite elements predictions observed in the glass transition frequency range are enhanced as the ratio  $\frac{G_g}{G_r}$

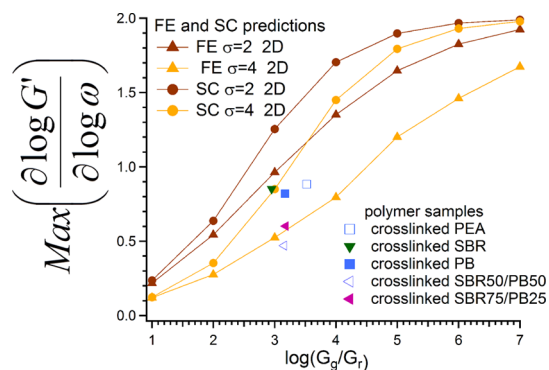


**Figure 9.** Maximum of  $\frac{\partial \log(G')}{\partial \log(\omega)}$  variation as a function of  $\log\left(\frac{G_g}{G_r}\right)$  for finite element method (FE) and the self-consistent approximation (SC). Data deduced from mechanical measurements performed on various polymer are plotted: cross-linked poly ethyl acrylate,<sup>32</sup> cross-linked styrene–butadiene copolymer, cross-linked polybutadiene,<sup>24</sup> and blends of SBR and PB chains (50% and 75% in weight of SBR).<sup>24</sup>

increases. Figure 10 compares the frequency dependence of the 2D macroscopic complex modulus predicted by the self-consistent and the finite element approaches. Results were obtained taking a constant time distribution width  $\sigma = 2$  and varying  $G_r$  values taken equal to  $10^{-5}G_g$ ,  $10^{-3}G_g$  and  $10^{-1}G_g$ . We observe that the larger the contrast between  $G_g$  and  $G_r$  moduli, the larger the difference between the finite element method and the self-consistent approximation. This discrepancy appears for  $\omega\tau_{\max} = 1$  and extends toward low frequencies as  $\frac{G_g}{G_r}$  increases. For  $\log\left(\frac{G_g}{G_r}\right) = 5$ , deviations are significant until  $\omega\tau_{\max} = 10^{-6}$ .

In Figure 9, we observe that the maximum value of the elastic modulus slope increases with the modulus contrast  $\log\left(\frac{G_g}{G_r}\right)$ . At high values of  $\log\left(\frac{G_g}{G_r}\right)$ ,  $\max\left(\frac{\partial \log(G')}{\partial \log(\omega)}\right)$  tends toward 2, which is the limit value corresponding to the slope of a purely Maxwellian response. At intermediate  $\log\left(\frac{G_g}{G_r}\right)$  values, the maximum slope predicted by the finite element method is smaller than the one given by the self-consistent approximation.

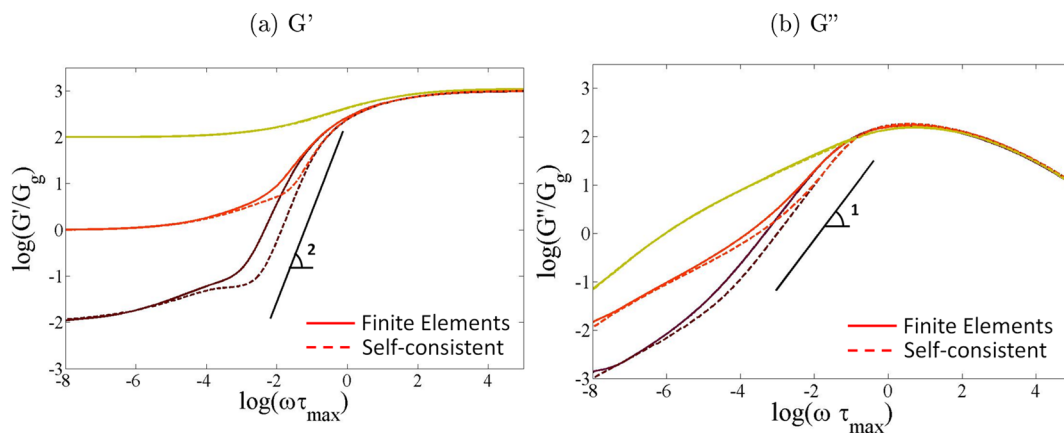


**Figure 10.**  $G'$  and  $G''$  calculated by finite element and self-consistent methods for  $\sigma = 2$  and  $\log\left(\frac{G_g}{G_r}\right) = 1$  (yellow),  $\log\left(\frac{G_g}{G_r}\right) = 3$  (red), and  $\log\left(\frac{G_g}{G_r}\right) = 5$  (brown).

In summary, all these results prove that the self-consistent method is reasonably accurate for predicting the viscoelastic modulus of heterogeneous systems, when compared to series and parallel methods. However, in the glass transition regime, it predicts a viscoelastic modulus significantly different from the one predicted by FE simulations for a highly heterogeneous polymer system (i.e., having a large time distribution  $\sigma$  and a high modulus contrast  $\frac{G_g}{G_r}$ ). We will analyze in detail the origins of this discrepancy in what follows.

We will now analyze the local mechanical response of such heterogeneous systems.

#### Spatial Organization of the Stress Relaxation Kinetics.

The main advantage of the finite element method is to provide maps of local stress or strain over the whole sample at each step of the relaxation process. It can thus evidence possible collective mechanisms of the relaxation process in the linear regime. Local stresses evolve mainly in a nonmonotonic way and can be negative. Figures 11 and 12 present both the local

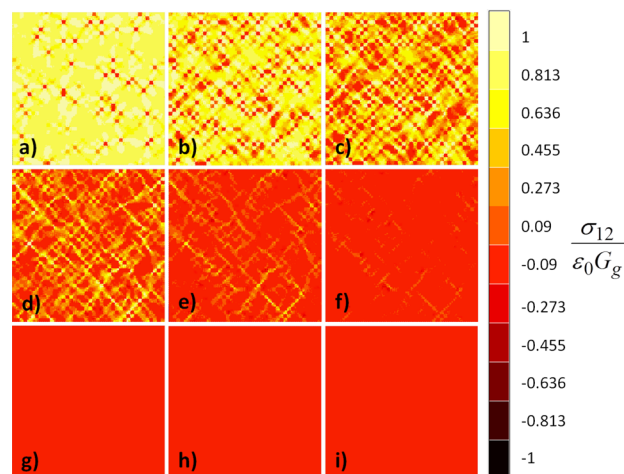


**Figure 11.**  $\sigma_{12}^i / \epsilon_0 G_g$  for different times of the macroscopic relaxation. Calculations were performed taking  $G_r = 10^{-3}G_g$ ,  $\sigma = 2$ , and (a)  $t^* = 3 \times 10^{-4}$ , (b)  $t^* = 10^{-2}$ , (c)  $t^* = 10^{-1}$ , (d)  $t^* = 1$ , (e)  $t^* = 10$ , (f)  $t^* = 40$ , (g)  $t^* = 400$ , (h)  $t^* = 10^4$ , or (i)  $t^* = 10^6$ . Color scale: pale yellow,  $\sigma_{12}^i = \epsilon_0 G_g$ ; black,  $\sigma_{12}^i = -\epsilon_0 G_g$ ; red,  $\sigma_{12}^i = 0$ .

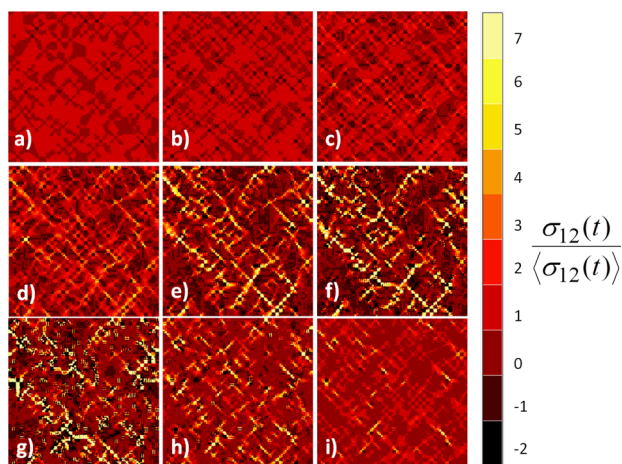


**Figure 12.** Maps of  $\frac{\sigma_{12}^i(t)}{\langle \sigma_{12}(t) \rangle}$  calculated taking  $G_r = 10^{-3}G_g$  and  $\sigma = 2$ . From left to right, the dimensionless time  $t/\tau_{\max}$  and average macroscopic stress  $\langle \sigma_{12}(t)/\tau_{\max} \rangle$  are equal to, respectively, (a) ( $3 \times 10^{-4}$ ,  $0.9\epsilon_0 G_g$ ); (b) ( $10^{-2}$ ,  $0.7\epsilon_0 G_g$ ); (c) (0.1,  $0.45\epsilon_0 G_g$ ); (d) (1,  $0.2\epsilon_0 G_g$ ); (e) ( $10^1$ ,  $0.05\epsilon_0 G_g$ ); (f) (40,  $0.01\epsilon_0 G_g$ ); (g) ( $4 \times 10^2$ ,  $0.0002\epsilon_0 G_g$ ); (h) ( $1 \times 10^4$ ,  $5.10^{-5}\epsilon_0 G_g$ ); (i) ( $10^6$ ,  $2.10^{-5}\epsilon_0 G_g$ ).

stress maps for  $\sigma = 2$  and  $G_r = 10^{-3}G_g$ , but using two different scales. (The individual stress relaxations for various domains are displayed in Figure 13.) In Figure 11, the color scale represents

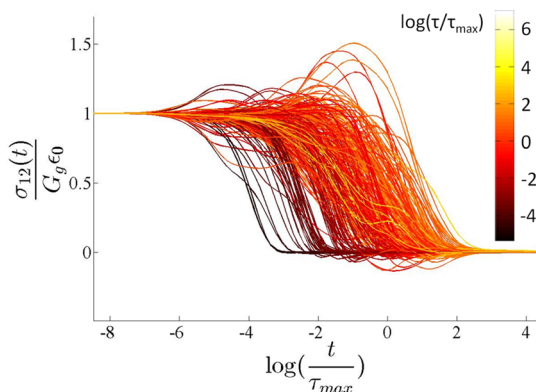


**Figure 13.** Local  $\frac{\sigma_{12}^i(t)}{G_g \epsilon_0}$  in each element as a function of  $\log\left(\frac{t}{\tau_{\max}}\right)$ . Simulations were performed taking  $G_r = 10^{-3}G_g$  and  $\sigma = 2$ .

the local stress  $\sigma_{12}^i(t)/G_g \epsilon_0$ . As a consequence, when all the blocks have a stress smaller than a tenth of their initial values,  $\sigma_{12}^i(t)/G_g \epsilon_0 < 0.1$ , the color is uniform (red). In contrast, in Figure 12, the local stresses are divided by the  $\sigma_{12}$  space average  $\langle \sigma_{12}(t) \rangle$ . Thus, the color scale is different for each time  $t$  and is normalized so that the color scale is calculated as a function  $\sigma_{12}^i(t)/\langle \sigma_{12}(t) \rangle$ . The yellow color corresponds to a stress which is ten times larger than the average one at a given time  $t$ . Maps obtained for the same macroscopic relaxation times are presented in Figures 11 and 12 and have the same label for panels a–i.

As seen on these figures, different behaviors are observed during the relaxation. We will thus divide the relaxation into four successive stages as described below. As a global reminder, we impose that the macroscopic strain and the microscopic moduli of each domain vary with time following their own intrinsic relaxation time.

*Stage 1: Uncoupled relaxations of domains.* At the beginning of the stress relaxation (i.e., typically  $t^* \sim 3 \times 10^{-4}$  and  $G(t) \approx 0.9G_g$  in Figure 2), corresponding to panel a in Figures 11 and 12), each domain evolves independently. The fastest domains ( $\tau_i < t$ ) first have a modulus smaller than the surrounding glassy matrix composed by the other domains. They are soft and cost nothing energetically to deform, but they are embedded in a glassy matrix; they cannot deform too much because it would deform the matrix. They typically behave as soft Eshelby inclusions in a hard matrix with a local strain  $\epsilon_{12} = 2\epsilon_0$  (cf. Figure 14a). In Figure 11a,b they appear in red in a glassy

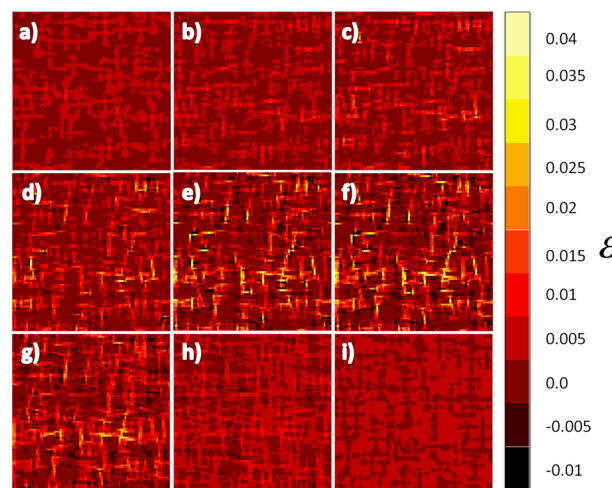


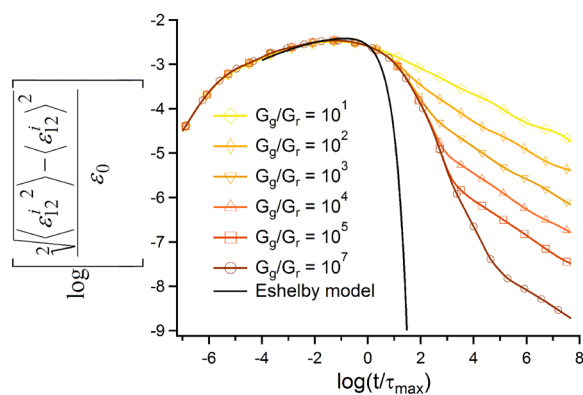
**Figure 14.** Maps of  $\epsilon$  calculated taking  $G_r = 10^{-3}G_g$ ,  $\sigma = 2$ , and  $\epsilon_0 = 0.01$ : (a)  $t^* = 3 \times 10^{-4}$ , (b)  $t^* = 10^{-2}$ , (c)  $t^* = 10^{-1}$ , (d)  $t^* = 1$ , (e)  $t^* = 10$ , (f)  $t^* = 40$ , (g)  $t^* = 400$ , (h)  $t^* = 10^4$ , and (i)  $t^* = 10^6$ .

matrix appearing in yellow. This means that their local stresses are very low. Then, the number of domains with a rubber modulus (termed “rubber domains” henceforth) increases, leading to a slow decay of the macroscopic stress. This phenomenon leads to an increasing standard deviation of strain in the system (cf. Figure 15b).

*Stage 2: The stress is supported only by a network composed of high modulus domains (“glassy network”).* As  $t$  increases, the number of domains supporting a glassy stress increases and coupling between neighboring domains begins to take place. Lines of high stress ( $\sigma_{12}$ ), oriented at  $45^\circ$  and  $-45^\circ$ , appear (cf. map c in Figures 11 and 12) and go through the whole sample forming a “glassy network”. These few domains support a high local stress of the order of  $\epsilon_0 G_g$  in yellow in Figure 11c–e. Figure 12 shows that they sustain a local stress which becomes much larger than the average stress. The density of these “glassy” domains decreases for increasing time  $t$  (cf. maps d–f in Figure 11) and is close to its percolation threshold at  $t$  around  $\tau_{\max}$  as displayed in Figure 11d. We have checked that, more generally, the stress lines of the glassy network are always parallel to the eigenvectors of the macroscopic strain tensor and that the strain lines are oriented at  $45^\circ$  of these eigenvectors.

Before depercolation of glassy domains, rubber inclusions still cannot deform too much because they remain embedded in the glassy network, the deformation of which has a high energetic cost. (cf. Figures 11 and 14, maps d and e). When a few domains of this glassy network relax their modulus, rubber zones can deform more and more (cf. Figure 14c–e). High deformation lines appear oriented at  $0^\circ$  and  $90^\circ$ . The location of these lines corresponds to the relaxing domains. This

(a) Stress standard deviation as a function of time for different  $G_r$ . From bottom to top  $\log(\frac{G_g}{G_r})$  goes from 7 to 1 with step unity. In black, the same curve if each element was independent and embedded in an homogeneous matrix.



(b) Strain standard deviation as a function of time for different  $G_r$ . From top to bottom  $\log(\frac{G_g}{G_r})$  goes from  $\infty$  to 1

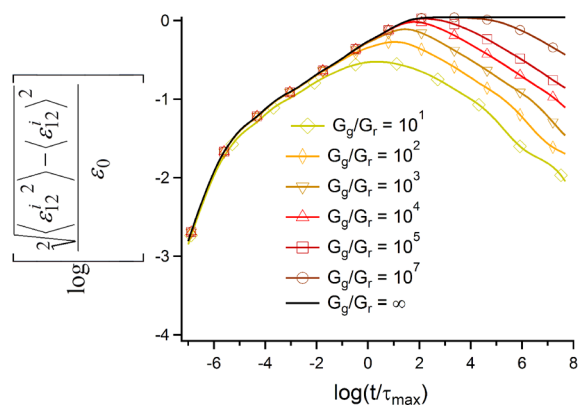


**Figure 15.** Evolution of stress and strain standard deviations with time.

phenomenon leads to a large and steep decrease of the macroscopic stress. In this regime, global stress relaxation is controlled by only the few “weak points” of the network relaxing their stress in a Maxwellian way because the energetic cost of deforming rubber domains is negligible compared to that necessary to deform these weak points. Only these few domains of this former “glassy” network have now a low modulus so that the network cannot sustain a high stress anymore. These few domains control the macroscopic relaxation of stress. This leads to a purely Maxwellian macroscopic relaxation in this range of times:  $G'$  and  $G''$  exhibit a characteristic  $\omega^2$  and  $\omega$  dependence, respectively, if  $G_r$  is sufficiently low (cf. Figures 5 and 6). When these domains are completely relaxed, the strain standard deviation is a maximum (cf. Figure 15b) because of high strain lines coexisting with glassy domains (cf. Figure 14g). When the macroscopic stress reaches the order of magnitude of  $10G_r\epsilon_0$ , the energetic cost of deforming a rubber domain is no more negligible compared to the global elastic energy, especially because they are now highly deformed; this is the beginning of stage 3.

*Stage 3: The stress is equally supported by the remaining “hard” network and the rubber matrix.* During this stage, rubber zones connecting glassy aggregates are still highly deformed so that the former glassy network is still visible in Figure 12g–i. This stage is characterized by an increasing number of rubber domains leading to smaller and smaller glassy aggregates and by a strain homogenization in the rubber zones to minimize the elastic energy. These two phenomena lead to a strain transfer (cf. Figure 14g,h) from rubber zones to the former glassy network so that the strain standard deviation decreases in Figure 15b. As a consequence of the strain transfer, the macroscopic stress can follow a pseudoplateau regime if the modulus contrast  $\frac{G_g}{G_r}$  is high (cf. blue curve in Figure 2, for example). This pseudoplateau is also visible in the self-consistent calculation for the same reasons (cf. Figure 10a).

*Stage 4: Uncoupled relaxation of the last hard domains.* Once the concentration of glassy aggregates becomes small, the relaxations of the last hard domains become uncoupled. They behave like hard Eshelby inclusions in a soft matrix (cf. map i in Figure 12). The macroscopic modulus relaxes slowly toward its rubber value.

## DISCUSSION

**Mechanical Coupling Induced by Dynamical Heterogeneities.** Figures 11 and 12 show that local stress is widely distributed during the macroscopic relaxation of a heterogeneous system. To characterize the amplitude of this stress disorder, we estimated the variance of the stress within the sample. In Figure 15, we have plotted the normalized variance of the stress as a function of time for  $\frac{G_g}{G_r}$  ratios varying from  $10^{-7}$  to  $10^{-1}$  (bottom to top). Disorder evolves during the whole process with a maximum during stage 2, i.e., in the time window where the glassy network is around its pseudopercolation threshold. Once the latter is crossed, the stress disorder is controlled by the mechanical contrast  $\frac{G_g}{G_r}$  and gradually decreases during stages 3 and 4.

The slow decay of the stress disorder during stage 3 and 4 is due to the heterogeneity of the matrix.

To get insight into the local stress relaxation disorder, we compare it to the stress variance predicted for the same domains but embedded in a homogeneous viscoelastic Maxwell matrix. In this classical Eshelby model, a straightforward calculation shows that the local stress undergone by a single domain or inclusion in the 2D geometry is given by the relation

$$\sigma_i = G_g \epsilon_0 e^{-t/\tau_{i,\text{eff}}^E} \text{ with } \tau_{i,\text{eff}}^E = \frac{2\tau_i \bar{\tau}}{\tau_i + \bar{\tau}} \quad (8)$$

where  $\tau_i$  is the local intrinsic relaxation time of the inclusion and  $\bar{\tau}$  is the time relaxation of the matrix. We assume here that the matrix and the inclusion have the same glassy modulus  $G_g$ . From relation 8 we compute the variance of the stress given by the same distribution of domains, i.e., with a relaxation time distribution given by  $p(\tau_i)$ . The stress variance predicted for a distribution of Eshelby inclusion is plotted in Figure 15 for comparison. At time  $t > 10\tau_{\text{max}}$ , the stress variance calculated from finite element simulations is many orders of magnitude larger than the one predicted for independent inclusions in a viscoelastic matrix. The coupling between domains is responsible for a huge disorder at the end of the relaxation.

It is worth noting that at short times, in stage 1, there is a good agreement between the independent inclusions model and the finite elements results, confirming there is no coupled domains relaxation.

According to the stress maps plotted in Figure 11, the stress levels are not randomly arranged within the sample. Indeed, high-stress lines are oriented at  $45^\circ$  from the strain eigendirections. These lines and their orientations are also observed for other strain geometries (incompressible sample undergoing a simple elongation or shear experiment performed on a compressible material). We deduce that the high-stress lines are oriented along the microscopic stress eigenvectors. We compute the 2D normalized correlation function  $I(r,t)$  of the stress in polar coordinates for each macroscopic relaxation time  $t$ .

$$I(r, t) = \frac{\langle \sigma(r+x, t) \sigma(x, t) \rangle_x - \langle \sigma(t) \rangle^2}{\langle \sigma(t)^2 \rangle - \langle \sigma(t) \rangle^2} \quad (9)$$

An example of the 2D normalized correlation of the stress in polar coordinates is presented in Figure 16. We observed that  $I(r,t)$  varies with  $\theta$  as  $\cos(4\theta) g(r,t)$ .

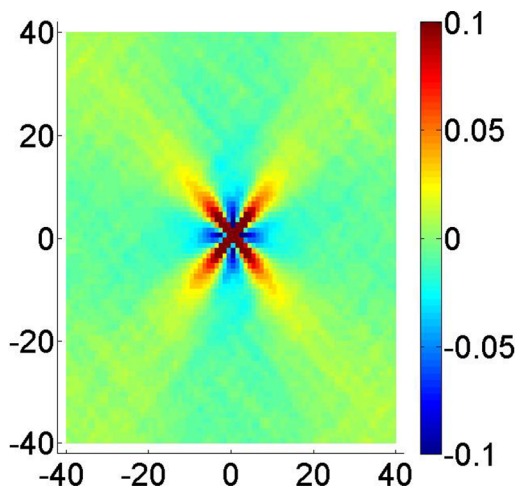
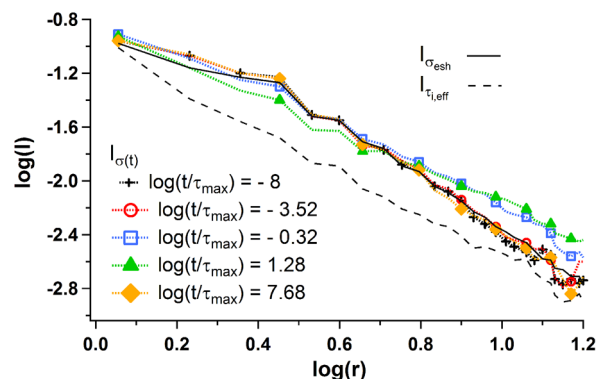


**Figure 16.** Example of the 2D normalized correlation function  $I(r,t)$  of the stress calculated from stress map d in Figure 11 taking  $G_r = 10^{-3}G_g$  and  $\sigma = 2$ .

The function  $g(r,t)$  is plotted in Figure 17 for various  $t$  values.  $g(r,t)$  scales as  $1/r^2$  in stages 1, 3, and 4 of the macroscopic relaxation in agreement with the  $g(r,t)$  scaling predicted for a single inclusion and as observed by Lemaître in simulation of supercooled viscous liquids.<sup>33</sup> However, at the middle of the macroscopic relaxation, i.e., in stage 2,  $g(r,t)$  varies like  $r^\beta$ , where  $\beta$  is larger than  $-2$  and reaches a maximum of the order of  $-1.3$ . This indicates, following the Lemaître discussion,<sup>33</sup> that the correlation length of the stress exceeds the size of the sample during stage 2, confirming the existence of a long-range correlation of the structure reminiscent of a percolation transition. This spatial correlation results from the elastic coupling between domains that induces correlation of the kinetics of stress relaxations.

**Local Effective Relaxation Times.** Elastic couplings create a spatial arrangement of the local stress that cannot be described in a mean field description. In that case, each domain is surrounded by a homogeneous matrix. We deduce that elastic interactions do modify the kinetics of the stress relaxation of

(a) Evolution of  $\log(I(r))$  as a function of  $\log(r)$  for different times of the relaxation



(b) Evolution of the slope of  $\log(I(r))$  as a function of  $\log(r) - \beta$  between  $\log(r) = 0.8$  and  $\log(r) = 1.1$  during the relaxation.

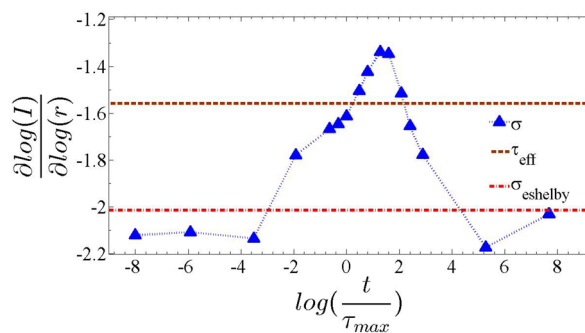


**Figure 17.** Spatial correlation of stress for different times of the relaxation.

each domain. In the following, the latter will be compared to the one of a Maxwell element having a relaxation time  $\tau_r$ . In this aim, we will attempt to define an effective relaxation time for each domain.

If the stress  $\sigma_{12}^i(t)$  decays exponentially, its relaxation time can be calculated by the integral of  $\sigma_{12}^i(t)$ :

$$\tau_\sigma = \int \frac{\sigma_{12}^i(t) - G_r \epsilon_0}{G_g} dt \quad (10)$$

However, if  $G_r \neq 0$ , it is easy to show that eq 10 leads to  $\tau_\sigma = \tau_i$  whatever the dynamical disorder of the surrounding domain.

Thus, the effective time defined by eq 10 is not relevant to discuss the complex kinetics of stress relaxation. The relation  $\tau_\sigma = \tau_i$  originates from the fact that the integral can be dominated by the slowest contributions of the local relaxation, which can be a very slow process. Indeed, most of the stress release of domains occurs during stage 2. However, in stages 3 and 4, the part of the relaxation is very long because of the strain balancing occurring between hard and rubber domains. Despite its small amplitude as compared to stage 2, this last part of the local relaxation dominates in eq 10.

To study the relaxation occurring in stage 2, we focus on the time for which each domain has relaxed its glassy stress by 1 order of magnitude. We thus collected the first time  $t_i^*$  at which  $\sigma_{12}^i(t_i^*)/G_g \epsilon_0$  becomes smaller than a given stress threshold  $\Sigma$ . We deduced the corresponding effective time  $\tau_{i,eff}$ . The latter is

defined as the characteristic relaxation time that a Maxwell element should have in order to reach at the time  $t_i^*$  the stress level  $\sigma_{12}^i(t_i^*)$ . Comparing the stress decay to an exponential one  $\sigma_{12}^i(t^*) = \Sigma \epsilon_0 G_g = \epsilon_0 G_g e^{-t^*/\tau_{i,\text{eff}}}$ , we define an effective relaxation time by  $\tau_{i,\text{eff}} = t_i^*/\ln(\epsilon_0 G_g/\Sigma)$ . Because we focus on the beginning of the macroscopic relaxation, the stress threshold  $\Sigma$  is chosen as the macroscopic stress level reached near the pseudopercolation threshold of glassy domains within the sample, i.e.,  $\Sigma \approx \epsilon_0 G_g/10$  (in Figure 2,  $G(t) = G_g/10$  at  $t \approx \tau_{\text{max}}$ ).

Figure 18 presents the  $\tau_{i,\text{eff}}/\tau_{\text{max}}$  values measured applying this procedure. Data obtained for different time distribution widths  $\sigma$  and  $G_r$  values are displayed as a function of  $\tau_i/\tau_{\text{max}}$ .

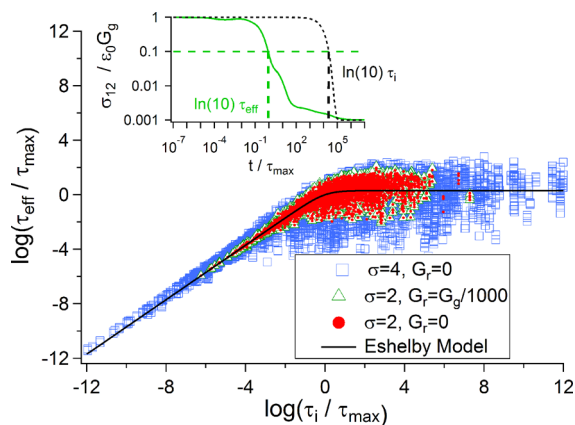


**Figure 18.** Variation of the effective relaxation times  $\tau_{i,\text{eff}}/\tau_{\text{max}}$  as a function of  $\tau_i/\tau_{\text{max}}$  (log–log plot). The effective relaxation times were determined applying the cut off method:  $\tau_{i,\text{eff}} = t^*/\ln(10)$  with  $\sigma_{12}^i(t^*) = \epsilon_0 G_g/10$  (cf. insert where the stress relaxation of a domain in the relaxing heterogeneous system (in green) is compared to the one of the same domain would undergo if it were alone). Results obtained for different values of  $G_r$  and  $\sigma$  are displayed: blue squares,  $\sigma = 4$  and  $G_r = 0$ ; green triangles,  $\sigma = 2$  and  $G_r = 10^{-3}G_g$ ; red circles,  $\sigma = 2$  and  $G_r = 0$ . The effective relaxation time of an inclusion having an intrinsic characteristic time  $\tau_i$  in an infinite homogeneous matrix whose  $\tau_{\text{max}}$  is the characteristic relaxation time is reported in black.

- At low  $\tau_i$ , the effective relaxation time is of the order of  $2\tau_i$ . The relaxation of the shortest  $\tau_i$  domains is thus slightly slower than that of isolated domains.

- At large  $\tau_i$ ,  $\tau_{i,\text{eff}}$  is significantly shorter than  $\tau_i$  and fluctuates around a limit value of the order of  $\tau_{\text{max}}$  with a standard deviation which is proportional to  $\sigma$ , the width of  $p(\tau)$ .

The crossover between the two regimes is broad and occurs at  $\tau_i$  values ranging between  $\tau_{\text{max}}$  and  $10\tau_{\text{max}}$ . Similar results are observed for a larger time distribution width; data obtained for  $\sigma = 4$  are displayed in Figure 18. Figure 18 shows that eq 8 describes well the average value of  $\tau_{i,\text{eff}}$  as a function of  $\tau_i$ .

We have computed the correlation function of the  $\tau_{i,\text{eff}}$  times. Data are displayed as dashed lines in Figure 17. As previously mentioned, the intrinsic times  $\tau_i$  are randomly drawn and are thus uncorrelated. As shown in Figure 17, the correlation function of  $\tau_{i,\text{eff}}$  scales with  $1/r^{1.5}$ , revealing that the slow relaxations are organized along high-stress lines. The domains located in high-stress lines have a stiff neighboring and can sustain a high local stress for a longer time. On the other hand, the slow domains that are outside the glassy stress lines are embedded in a soft matrix. Their relaxation kinetics is similar to that of the matrix.

In summary, at half course of relaxation (stage 2), a long-range correlation appears both in the stress field and in the kinetics of local relaxations, revealing that domains have coupled the release of stress. Simultaneously, at a macroscopic scale, the viscoelastic modulus shows a quasi-Maxwellian behavior. We will now compare the kinetics of local relaxations to that of macroscopic modulus decrease.

**Comparing Relaxation Time Distributions.** Lastly, we compare the stress relaxation of domains with the macroscopic one. We compute the distribution function of the effective relaxation times  $P_{\text{eff}}(\tau_{i,\text{eff}})$  corresponding to the data of Figure 18. This time distribution accounts only for the relaxation from the glassy modulus to one tenth of its initial value. We see that  $P_{\text{eff}}(\tau_{i,\text{eff}})$  drops toward zero for times  $t$  larger than  $t_c = 10^2\tau_{\text{max}}$ , i.e., at the end of stage 2 contrary to the intrinsic time distribution  $P(\tau_i)$  (cf. Figure 19). We compared  $P_{\text{eff}}(\tau_{i,\text{eff}})$  to the time distribution  $F(\tau)$  associated with the macroscopic viscoelastic relaxation deduced from eq 6.

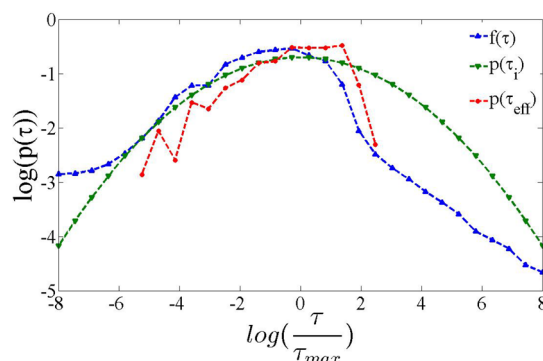


**Figure 19.** Effective time distribution  $P_{\text{eff}}(\tau_{i,\text{eff}})$  in red, rheological time distribution  $F(\tau)$  in blue, and intrinsic time distribution  $P(\tau_i)$  in green.

We observe that  $F(\tau)$  strongly decreases at the pseudopercolation threshold ( $\tau \sim 10\tau_{\text{max}}$ ) as  $P_{\text{eff}}(\tau_{i,\text{eff}})$  does in this time range. The main differences between  $F(\tau)$  and  $P_{\text{eff}}(\tau_{i,\text{eff}})$  are observed for  $t > 100\tau_{\text{max}}$ . Within this time window,  $F(\tau)$  is smaller than  $P(\tau_i)$  and remains nonzero. Obviously, given the chosen stress threshold,  $P_{\text{eff}}(\tau_{i,\text{eff}})$  cannot capture this regime.  $F(\tau)$  contains a tail of long relaxation times that originates from the persistence of the percolation network at long times as discussed above.

**Summary.** We have identified four main steps whose main features are summed up in Figure 20 both at a local and at a macroscopic level. First, at the beginning of the relaxation, stage 1, isolated fast domains relax in a glassy matrix with a characteristic time close to their intrinsic relaxation time. The Palierne self-consistent model describes precisely the relaxation, as can be seen in Figure 8. Then in stage 2, the macroscopic relaxation becomes slower than the one predicted by the self-consistent approach, owing to the heterogeneity of the matrix. At a mesoscopic scale, the domains aligned on the principal stress directions show a correlated decay (cf. Figure 17). Because the stress is supported by lines composed of slow domains, the disorder of local stresses and effective relaxation times is then larger than the one expected assuming a mean field approximation (cf. Figure 15). Hereafter, these glassy stress lines break up and the relaxation becomes very steep and follows a characteristic Maxwellian relaxation for the viscoelastic modulus. In stage 3, few slow domains support a local stress, of the order of  $10\epsilon_0 G_r$ , that is higher than the

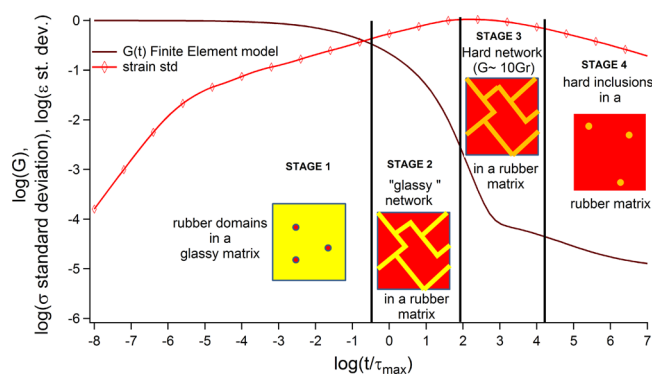


**Figure 20.** Four main regimes of the macroscopic modulus time relaxation of a glassy polymer. The modulus predicted by the finite element method (brown full line) is plotted for  $\sigma = 2$  and  $G_r = 10^{-5}G_g$ . Corresponding strain variance (red open diamonds) is plotted. Schematic local stress arrangements are displayed for each step of the macroscopic relaxation.

average macroscopic stress. On the other hand, the fastest domains are in the rubber state. The slowest domains form a “hard” network that supports partly the sample stress. Their relaxation is slowed by strain transfer from the highly deformed matrix toward the hardest domains and induces a pseudoplateau regime for the macroscopic modulus. At the end of this strain transfer, some of the slowest domains reach the rubber state, which leads to the destruction of the hard network. In stage 4, the slowest domains form aggregates embedded in a rubber matrix. Their relaxation leads to a slow decay of the macroscopic modulus that is also very well-captured by the Palierne self-consistent model (Figure 8).

## CONCLUSION

Polymers in the glassy regime are known to exhibit large dynamical heterogeneities. Using finite element simulations, we have predicted the viscoelastic response of 2D glasses whose widths of intrinsic time distribution vary between 4 and 8 decades, as for real 3D glassy polymers. We have considered only log-normal time distributions. We show that dynamical heterogeneities induce a strong inhomogeneous stress field that evolves with time in a complex way. By means of FE simulations, we have identified the cascades of local processes occurring during the macroscopic relaxation.

Long-range mechanical couplings acting between neighboring domains control both the local stresses and their relaxation kinetics. For instance, we observed that the domains with the longest intrinsic times prematurely release most of their stress when their neighbors have relaxed. The exponent of the spatial correlation of the stress decay is at a maximum for a macroscopic relaxation time close to the mean time of the intrinsic time distribution. Therefore, the stress correlation length is larger than the sample size. At stage 2 of the macroscopic relaxation, glassy paths remain in the sample oriented along the direction of the principal axis of the stress. This time corresponds to the vicinity of a percolation threshold. The network of high modulus domains supports most of the macroscopic stress. As a consequence, the local relaxation of the fastest domains participating in the “glassy” network induces a strong decrease of the sample stress and controls it.

As a result, the time decay of macroscopic stress is nearly Maxwellian. It remains so until the stress sustained by the network becomes ten times larger than that undergone by the

matrix. At that point, a pseudoplateau regime can occur if  $\sigma \leq 2.5$  and  $\log \frac{G_r}{G_g} \geq 4$ . A slow decay of the stress follows until every domain enters a rubber state; the rubber plateau is then reached.

Remarkably, the self-consistent model captures most of the trends of this behavior but underestimates the role of correlations, and as a consequence, the model highly reduces the long-time portion of the viscoelastic spectrum. However, the modulus predicted by a mean field approach can thus be up to 1000 times smaller than the value given by a FE simulation in the glass transition zone.

We believe that these FE results are very important in order to quantitatively understand the polymer viscoelastic spectrum. Quantitative modeling in this frequency domains is still an important challenge, especially in the crossover domain in which Rouse modes are expected to coexist with the slow modes of the  $\alpha$  relaxation. Otherwise, this work shows that the rheological and the intrinsic time spectrum are very different from each other; the longer time part of the rheological spectrum is considerably reduced compared to the intrinsic one. We believe that this phenomenon should also be relevant to both calorimetry and dielectric relaxation experiments, but likely quantitatively different because the averaging of intrinsic relaxation times is different. Lastly, our results show that the maximum slope of the frequency dependence of the elastic modulus provides an accurate measurement of the width of the dynamical heterogeneities distribution. According to a rough first comparison between 2D FE simulations and experimental results, the standard deviation of the intrinsic time distributions should be close to 2 for homopolymers while it would be larger (up to a value close to 4) for asymmetric miscible polymer blends. In a further step, it should be possible to compare the intrinsic time distribution deduced from rheological measurements to that measured by other methods, such as differential scanning calorimetry or dielectric experiments. Finally, using FE simulations, it should be possible to predict the mechanical response of polymer systems whose dynamical heterogeneities are known from other experiments. This would be helpful, for instance, in predicting the relation between the structure of asymmetric miscible blends or interpenetrated networks and their mechanical properties close to the glass transition.

## AUTHOR INFORMATION

### Corresponding Author

\*E-mail: [helene.montes@espci.fr](mailto:helene.montes@espci.fr)

### Notes

The authors declare no competing financial interest.

## REFERENCES

- (1) Ward, I. M. *Structure and Properties of Oriented Polymers*; Springer Science & Business Media: Dordrecht, The Netherlands, 1997.
- (2) Ediger, M. D. *Annu. Rev. Phys. Chem.* **2000**, *51*, 99–128.
- (3) Richert, R. J. *J. Phys.: Condens. Matter* **2002**, *14*, R703–R738.
- (4) Schmidt-Rohr, K.; Spiess, H. *Macromolecules* **1991**, *24*, 5288–5293.
- (5) Tracht, U.; Wilhelm, M.; Heuer, A.; Feng, H.; Schmidt-Rohr, K.; Spiess, H. W. *Phys. Rev. Lett.* **1998**, *81*, 2727–2730.
- (6) Reinsberg, S. A.; Qiu, X. H.; Wilhelm, M.; Spiess, H. W.; Ediger, M. D. *J. Chem. Phys.* **2001**, *114*, 7299–7302.
- (7) Cicerone, M. T.; Blackburn, F. R.; Ediger, M. D. *Macromolecules* **1995**, *28*, 8224–8232.
- (8) Hwang, Y.; Inoue, T.; Wagner, P. A.; Ediger, M. D. *J. Polym. Sci., Part B: Polym. Phys.* **2000**, *38*, 68–79.

- (9) Cicerone, M. T.; Wagner, P. A.; Ediger, M. D. *J. Phys. Chem. B* **1997**, *101*, 8727–8734.
- (10) Lee, H.-N.; Riggleman, R. A.; de Pablo, J. J.; Ediger, M. D. *Macromolecules* **2009**, *42*, 4328–4336.
- (11) Riggleman, R. A.; Lee, H.-N.; Ediger, M. D.; De Pablo, J. J. *Phys. Rev. Lett.* **2007**, *99*, 215501.
- (12) Riggleman, R. A.; Lee, H.-N.; Ediger, M. D.; de Pablo, J. J. *Soft Matter* **2010**, *6*, 287–291.
- (13) Papakonstantopoulos, G. J.; Riggleman, R. A.; Barrat, J.-L.; de Pablo, J. J. *Phys. Rev. E* **2008**, *77*, 041502.
- (14) Riggleman, R. A.; Schweizer, K. S.; de Pablo, J. J. *Macromolecules* **2008**, *41*, 4969–4977.
- (15) Dequidt, A.; Long, D. R.; Sotta, P.; Sanseau, O. *Eur. Phys. J. E: Soft Matter Biol. Phys.* **2012**, *35*, 61.
- (16) Long, D.; Lequeux, F. *Eur. Phys. J. E: Soft Matter Biol. Phys.* **2001**, *4*, 371–387.
- (17) Chen, K.; Saltzman, E. J.; Schweizer, K. S. *J. Phys.: Condens. Matter* **2009**, *21*, 503101.
- (18) Yoshimoto, K.; Jain, T. S.; Workum, K. V.; Nealey, P. F.; de Pablo, J. *Phys. Rev. Lett.* **2004**, *93*, 175501.
- (19) Sillescu, H. *J. Non-Cryst. Solids* **1999**, *243*, 81–108.
- (20) Gudmundson, P. *European Journal of Mechanics a-Solids* **2006**, *25*, 379–388.
- (21) Iesan, D.; Quintanilla, R. *Mech. Res. Commun.* **2013**, *48*, 52–58.
- (22) Tang, S.; Greene, M. S.; Liu, W. K. *J. Mech. Phys. Solids* **2012**, *60*, 199–226.
- (23) Merabia, S.; Long, D. *Eur. Phys. J. E: Soft Matter Biol. Phys.* **2002**, *9*, 195–206.
- (24) Shi, P.; Schach, R.; Munch, E.; Montes, H.; Lequeux, F. *Macromolecules* **2013**, *46*, 3611–3620.
- (25) Ferry, J. D. *Viscoelastic Properties of Polymers*; John Wiley & Sons: New York, 1980; pp 348–349.
- (26) Nemat-Nasser, S.; Hori, M. *Micromechanics: Overall Properties of Heterogeneous Materials*; Elsevier: Amsterdam, 1999; Vol. 2.
- (27) Masson, R.; Zaoui, A. *J. Mech. Phys. Solids* **1999**, *47*, 1543–1568.
- (28) Palierne, J. *Rheol. Acta* **1990**, *29*, 204–214.
- (29) Jean, A.; Willot, F.; Cantournet, S.; Forest, S.; Jeulin, D. *Int. J. Multiscale Comput. Eng.* **2011**, *9*, 271–303.
- (30) Z-Set. <http://www.zset-software.com/>.
- (31) Ryckelynck, D.; Vincent, F.; Cantournet, S. *Comput. Meth. Appl. Mech. Eng.* **2012**, *225*, 28–43.
- (32) Berriot, J.; Montes, H.; Lequeux, F.; Long, D.; Sotta, P. *Macromolecules* **2002**, *35*, 9756–9762.
- (33) Lemaitre, A. *Phys. Rev. Lett.* **2014**, *113* (24), 245702.